ChemComm

COMMUNICATION

View Article Online
View Journal

Cite this: DOI: 10.1039/d6cc01824f

Received 26th March 2026,
Accepted 23rd April 2026

DOI: 10.1039/d6cc01824f

rsc.li/chemcomm

Dipole-field interaction: a missing link to bridge the gap between theoretical and experimental catalysis in single-atom electrocatalysts for CO_2 reduction

Ruirui Ren,[a] Yuhang Wang, *[ab] Bo Li *[a] and Jun Fan *[b]

The CO_2-to-CO reduction behaviour on Fe/Co/Ni-based single-atom catalysts was systematically investigated. *CO is preferentially stabilized relative to *COOH under increasingly negative interfacial electric fields. A pH-dependent volcano relationship is revealed, exhibiting a rightward shift with increasing pH due to the distinct dipole moments of *CO and *COOH. Benchmarking against experimental data validates the microkinetic volcano model and identifies promising catalyst candidates. Importantly, dipole–field interactions emerge as a general descriptor, bridging theoretical predictions and experimental observations in CO_2RR and beyond.

Electrocatalytic conversion of CO_2 into value-added chemicals is regarded as a promising strategy for achieving carbon neutrality, particularly when driven by renewable energy sources.[1–8] Among various CO_2 reduction products, CO has attracted considerable attention due to its industrial scalability. Although significant progress has been made in CO_2-to-CO conversion, the catalytic performance remains insufficient for practical applications.[9,10] Therefore, developing CO_2 reduction catalysts with enhanced activity, selectivity, and stability remains a critical challenge in the field.

Single-atom catalysts (SACs) have attracted extensive attention due to their tuneable coordination environments, unique electronic structures, and high atomic utilization efficiency.[11–14] Through large-scale data mining analysis, as shown in Fig. 1a, we found that Fe/Co/Ni-based single-atom catalysts dominate the reported systems, accounting for as much as 78.5% (data source: *DigCat*,[15] data up to January 2026). Further statistical analysis indicates that Fe/Co/Ni-based SACs generally exhibit favourable CO selectivity, with faradaic efficiencies (FE) typically exceeding 75% (Fig. 1b). These results provide important experimental evidence and data support for the rational design of catalysts with high CO selectivity. However, the catalytic activity of single-atom catalysts strongly depends on their electronic structures,[16] while the chemical diversity of SACs poses significant challenges in the systematic exploration of potential high-performance catalysts.

Theory-driven catalyst design can significantly shorten the development cycle of high-performance catalysts.[17] However, the predictive capability of conventional theoretical approaches in catalyst screening remains limited, as they usually capture only relative reaction trends rather than quantitative activity metrics. This limitation mainly arises because CO_2 reduction under realistic electrochemical conditions is referenced to the reversible hydrogen electrode (RHE) and exhibits pronounced pH dependence.[18,19] In traditional computational frameworks, pH effects are often treated as constant corrections to reaction free energies, which neglect the dynamic influence of electrode potential and electrolyte environment. Such simplifications fail

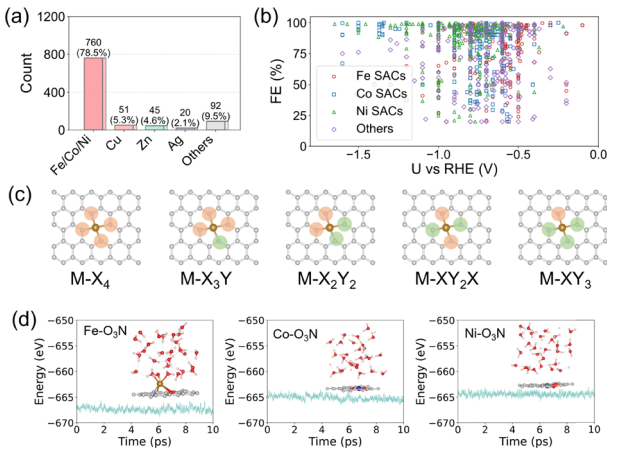

Fig. 1 Large-scale data mining and structural features of single-atom catalysts. (a) Frequency distribution of metal elements in reported SACs. (b) Relationship between applied potential (*U vs.* RHE) and faradaic efficiency (FE) for CO production on SACs. (c) Schematic illustration of different coordination environments, where M = Fe, Co, Ni and X = B, C, N, O. (d) Thermodynamic stability of the M–O_3N configuration evaluated using AIMD simulations.

[a] *College of Chemistry and Pharmaceutical Engineering, Nanyang Normal University, Nanyang 473061, PR China*

[b] *Department of Materials Science and Engineering, City University of Hong Kong, Hong Kong, 999077, China*

to accurately describe the dipole–field interactions between adsorbed intermediates and the interfacial electric field under operating conditions, thereby compromising the accuracy of theoretical predictions.[20] Therefore, there is an urgent need to develop high-precision theoretical models that can explicitly capture electrochemical interfacial effects and pH-dependent behaviour, in order to guide the rational design and targeted synthesis of advanced CO_2RR catalysts.

In this work, we systematically investigated the CO_2 reduction performance of Fe-, Co-, and Ni-based SACs with 135 distinct nonmetal coordination environments using theoretical calculations. Our results reveal the physical origin of the electric-field-induced shift in volcano plots under electrochemical conditions. By benchmarking against experimental data, we further validate the reliability and predictive capability of the microkinetic volcano model. These findings provide important theoretical insights and guidance for the rational design of high-performance CO_2RR catalysts. Moreover, through a comparative analysis of dipole–field interactions in the $*NO_3^-$ and $*HNO_3$ species, we demonstrate the universality of dipole–field effects, indicating that they can serve as a crucial bridge between theoretical predictions and experimental observations.

Structure and stability. The catalysts investigated in this work involve four types of coordination atoms (B, C, N, and O), leading to five representative coordination configurations (Fig. 1c). The construction procedure and detailed lattice parameters of the Fe/Co/Ni-based SACs are provided in the SI and Fig. S1. Previous studies have demonstrated that an increase in the oxygen content in the coordination environment generally results in higher formation energies, among which the M–O_4 configuration exhibits relatively high formation energies.[21] This behaviour can be mainly attributed to the limited availability of empty orbitals provided by oxygen atoms and their relatively weak electron-accepting capability, which restricts the stabilization of highly coordinated structures. Thus, the M–O_3N configuration was selected as a representative model to systematically explore the thermodynamic stability of different SACs. As shown in Fig. 1d, *ab initio* molecular dynamics (AIMD) simulations were performed for three single-atom systems at 500 K. The results reveal only minor fluctuations in total energy, with no evident bond breaking or formation, indicating good thermal stability at elevated temperatures. Moreover, snapshots extracted from the AIMD trajectories show that the single atoms remain firmly anchored on the graphene substrate. These results collectively demonstrate that the designed SACs exhibit favourable thermodynamic and structural stability, providing a solid theoretical foundation for their potential experimental synthesis.

Dipole-field interaction and thermodynamic volcano. The presence of interfacial electric fields can markedly modulate the adsorption strength of reaction intermediates through dipole–field interactions.[20] Fig. 2a–c present the electric-field response characteristics of *COOH and *CO on representative catalyst surfaces. The magnitude of the dipole moment determines the sensitivity of intermediates to external electric fields. Overall, *CO exhibits a larger dipole moment than *COOH, and

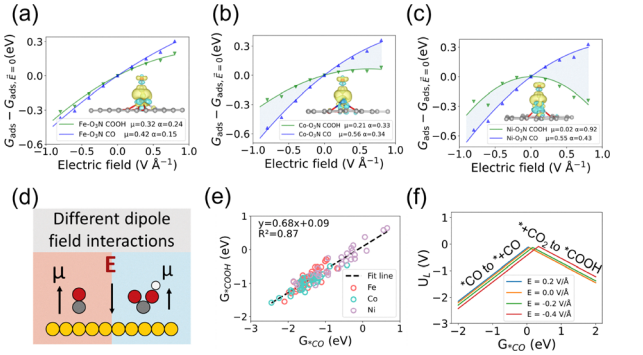

Fig. 2 Dipole–field interactions of *CO/*COOH and the thermodynamic volcano. (a)–(c) Electric-field effects on the adsorption free energies of *CO/*COOH on M–O_3N sites. Insets show charge density difference induced by *CO adsorption; yellow and teal isosurfaces denote electron accumulation and depletion, respectively. Atom colours: Fe (brown), Co (blue), Ni (light blue), C (gray), O (red), N (silver), H (light pink). (d) Schematic illustration of the dipole–field interactions of *CO and *COOH. (e) Scaling relationship between adsorption free energies of *CO (G_{*CO}) and *COOH (G_{*COOH}). (f) Electric-field-induced evolution of electrocatalytic thermodynamics volcano plot.

thus its adsorption energy shows a more pronounced dependence on the electric field. Specifically, under the same electric field strength, the adsorption stability of *CO is significantly enhanced, as illustrated in Fig. 2d. Charge redistribution analyses further reveal that CO adsorption is accompanied by more substantial charge transfer at the metal sites, indicating stronger electronic interactions between *CO and the active centres (Fig. 2a–c and Fig. S2).

Similar electric-field response trends for *CO and *COOH were observed on other representative SACs, as shown in Fig. S3, confirming the generality of the dipole–field interaction. Next, by systematically comparing the variations in M–C bond lengths (M denotes the metal site) under different electric fields (Fig. S4–S6), we uncovered the field-induced geometric evolution of the active sites. Taking Fe–O_3N as a representative example, when the electric field strength changes from +0.8 to −0.8 V Å^{-1}, the M–C bond length decreases from 1.765 Å to 1.728 Å. This bond contraction indicates stronger interactions, which are in line with the observed trends in adsorption energies.

During CO formation in CO_2 reduction, catalytic activity is highly sensitive to the free-energy changes of individual elementary steps. Owing to the distinct electric-field responses of *COOH and *CO, the free-energy difference $\Delta G = G_{*CO} - G_{*COOH}$ systematically shifts with the electric field, thereby modulating the thermodynamic driving force of the reaction. To establish a unified volcano model, we constructed a CO_2RR-to-CO thermodynamic volcano plot using *CO as the descriptor, based on the linear relationship between *COOH and *CO, together with averaged dipole moments and polarizabilities (summarized in Table S1 and Fig. S7). Based on scaling analysis in Fig. 2e, the resulting volcano plot is shown in Fig. 2f. With increasing interfacial electric field, the CO_2RR-to-CO volcano plot gradually shifts toward the right, indicating that the reaction system is accompanied by a pronounced change in the potential-determining step. Generally, CO_2RR conditions

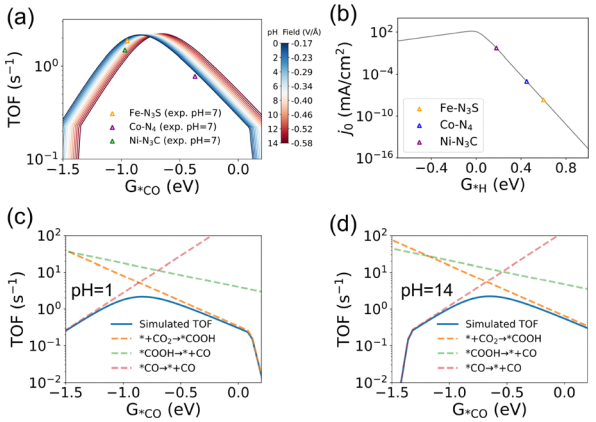

Fig. 3 pH-dependent volcano and rate-determining step analysis. (a) pH-dependent modelling of CO_2RR on single-atom catalysts at −1 V/RHE, where more negative electric fields correspond to alkaline conditions and less negative fields to acidic conditions. (b) Kinetic activity volcano for HER competition of M–N–C catalysts. (c) and (d) Rate-determining steps for CO formation under acidic and alkaline conditions.

correspond to negative electric fields.[22] Therefore, in the subsequent analysis, we focused on the activity changes within the negative electric field range. Taken together, although the thermodynamic volcano plot captures the overall trend of catalytic activity under varying electric fields, achieving quantitative prediction of catalytic performance requires further consideration of kinetic effects.

pH-dependent volcano. By comprehensively considering both kinetic and thermodynamic factors of the possible elementary steps in CO_2RR, we developed a pH-dependent theoretical framework. The results for calculating the point of zero charges (PZC) are presented in Fig. S8. The microkinetic simulations were performed following the methodology reported in our previous work[23,24] and detailed in the Supporting Information. Fig. 3a illustrates the pH-dependent volcano plots for CO_2RR-to-CO on Fe/Co/Ni-based single-atom catalysts at −1 V *vs.* RHE. The results reveal that, under realistic reaction conditions, the volcano plots systematically shift toward the right with increasing pH, which is consistent with the evolution trend predicted by the thermodynamic volcano model. Meanwhile, the sharp peak at the volcano apex gradually evolves into a smoother curve compared with Fig. 2f. This behaviour can be attributed to kinetic modulation induced by variations in intermediate surface coverage in the apex region.

To further validate the accuracy of the proposed volcano model, we performed a systematic benchmarking analysis. Several representative single-atom catalysts were selected for comparison,[25–27] as shown in Fig. 3a, and the results reveal a strong agreement between experimentally measured turnover frequencies (TOFs) and theoretical predictions, thereby confirming the reliability and predictive capability of the developed volcano model. Constant-potential density functional theory (DFT) calculations may accurately capture potential-dependent behavior,[28] while its treatment of pH effects *via* a constant correction (k_BT ln(10) pH) may sometimes lead to deviations under high-pH conditions due to dipole and polarizability effects. These findings further demonstrate that explicitly incorporating dipole–field interactions enable high-precision prediction of catalytic activity. Moreover, by evaluating the hydrogen evolution reaction (HER) activity of different catalysts (Fig. 3b), we provide theoretical insights into the intrinsic origin of the high activity and selectivity observed in benchmark catalyst systems, offering a mechanistic explanation for their superior performance.

To gain deeper mechanistic insights, we systematically analysed the reaction rates of individual elementary steps under both acidic and alkaline conditions (Fig. 3c and d). Owing to the distinct dipole–field interactions of different intermediates, the volcano plots under alkaline conditions exhibit an overall rightward shift.

In general, when G_{*CO} is sufficiently negative, CO desorption becomes the rate-determining step. Conversely, when G_{*CO} is positive, the linear scaling relationship between *CO and *COOH implies that G_{*COOH} is also typically positive; under such conditions, the formation of *COOH dominates the reaction kinetics and thus constitutes the RDS.

Taken together, the pH-dependent volcano model developed herein provides a new mechanistic framework for understanding CO_2RR-to-CO, effectively bridging the gap between theoretical predictions and experimental observations. Furthermore, based on the established volcano model, we predicted a series of promising single-atom catalysts with high catalytic activity across different pH conditions (Fig. S9). For instance, Co–CNON, Ni–BCBC, and Ni–OC_3 are located near the apex of the volcano plots under acidic, neutral, and alkaline conditions, respectively, suggesting their outstanding catalytic performance and offering valuable theoretical guidance for targeted experimental synthesis.

Generality of dipole-field interaction. Notably, a clear linear correlation between the adsorption free energies of NO_3^- and HNO_3 was first identified (Fig. 4a, R^2 = 0.74). This correlation suggests that $\Delta G(HNO_3^*)$ can be reasonably approximated by $\Delta G(NO_3^*)$, thereby effectively reducing the complexity of the reaction system. By further analysing the dipole responses of NO_3^- and HNO_3 under varying electric fields (Fig. 4b), we found that $*NO_3$ possesses a larger intrinsic dipole moment and thus exhibits a stronger and more pronounced field-dependent response. Additional calculations confirm the generality of dipole–field interactions for NO_3^- and HNO_3 on Fe-SACs (Fig. 4c), revealing that $*NO_3$ couples more strongly with the interfacial electric field than $*HNO_3$.

These results indicate that the intrinsic differences in charge distribution among reaction intermediates lead to distinct dipole moments and polarizabilities. In general, intermediates of similar nature tend to follow linear scaling relationships; however, variations in intrinsic dipole moments inevitably shift these relationships, thereby reconstructing and migrating the catalytic activity volcano plots.

Therefore, dipole–field interaction can be regarded as a critical "missing link" bridging theoretical calculations and experimental catalytic performance. Beyond CO_2 reduction,

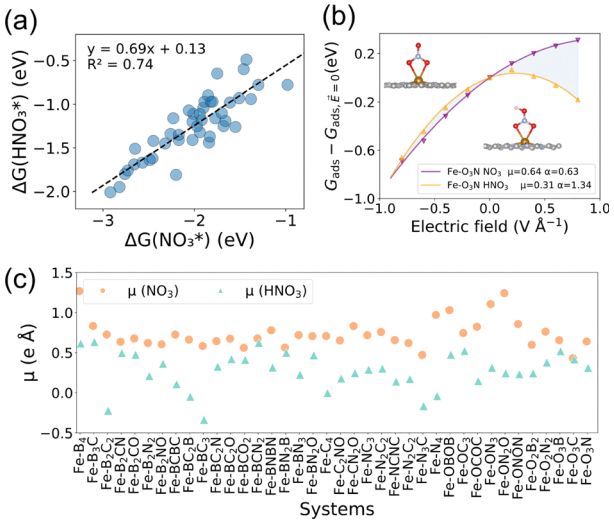

Fig. 4 Dipole–field interactions of key intermediates in NO_3RR. (a) Scaling relationship between the adsorption free energies of NO_3 $(\Delta G(NO_3^*))$ and HNO_3 $(\Delta G(HNO_3^*))$ on Fe-based single-atom catalysts. (b) Electric-field effects on the adsorption free energies of $*NO_3$ and $*HNO_3$ on $M–N_4$ sites (M = Fe, Co, Ni). Insets show charge density difference upon adsorption; yellow and teal isosurfaces indicate electron accumulation and depletion, respectively. (c) Dipole moments of $*NO_3$ and $*HNO_3$ on representative Fe-based catalysts.

this concept provides a universal theoretical framework for understanding and predicting activity trends in a broad range of electrocatalytic reactions.

In conclusion, this work systematically compares the dipole–field interactions of *CO and *COOH on SACs, revealing the decisive role of interfacial electric fields in governing CO_2RR mechanisms and activity. We show that (1) *CO exhibits stronger dipole–field interactions than *COOH; (2) their difference in intrinsic dipole moment drives a pronounced rightward shift of the CO_2RR-to-CO volcano; and (3) similar dipole effects are observed in NO_3RR, confirming the generality of this phenomenon. These results establish dipole–field interaction as a key descriptor for activity prediction and as an indispensable link for the efficient, theory-guided design of single-atom electrocatalysts.

Ruirui Ren: data curation/investigation/writing – original draft; Yuhang Wang: investigation/review/writing – review & editing; and Bo Li and Jun Fan: conceptualization/funding acquisition/supervision.

Conflicts of interest

There are no conflicts to declare.

Data availability

The data supporting the findings of this study have been included as part of the supporting information (SI) and are available from the corresponding author upon reasonable request. Supplementary information is available. See DOI: https://doi.org/10.1039/d6cc01824f.

Acknowledgements

This work was supported by the Hong Kong Research Grant Council Collaborative Research Fund C1017-22G and C1002-21G, City University of Hong Kong 7006111 and 7020112, and Science Foundation for Excellent Youth of Henan Province (212300410064).

References

1 Y. Wang, T. Liu and Y. Li, *Chem. Sci.*, 2022, **13**, 6366–6372.
2 Q. Chen, H. Yu, H. Li, K. Liu and M. Liu, *Chem. Commun.*, 2025, **61**, 19403–19420.
3 H. Wang, X. Kang and B. Han, *Chem. Soc. Rev.*, 2025, **54**, 10156–10244.
4 M. J. Sun, Z. W. Gong, J. D. Yi, T. Zhang, X. Chen and R. Cao, *Chem. Commun.*, 2020, **56**, 8798–8801.
5 Y. Yao, W. Zhuang, R. Li, K. Dong, Y. Luo, X. He, S. Sun, S. Alfaifi, X. Sun and W. W. Hu, *Chem. Commun.*, 2023, **59**, 9017–9028.
6 X. L. Xie, F. Chen, W. W. Wang, L. Y. Lyu, M. J. Sun, T. Zhang and R. Cao, *Chem. Commun.*, 2025, **61**, 13485–13488.
7 M. He, W. An, Y. Wang, Y. Men and S. Liu, *Small*, 2021, **17**, 2104445.
8 X. Cui, W. An, X. Liu, H. Wang, Y. Men and J. Wang, *Nanoscale*, 2018, **10**, 15262–15272.
9 H. Cao, Z. Zhang, J.-W. Chen and Y.-G. Wang, *ACS Catal.*, 2022, **12**, 6606–6617.
10 W. Yang, Z. Jia, B. Zhou, L. Chen, X. Ding, L. Jiao, H. Zheng, Z. Gao, Q. Wang and H. Li, *ACS Catal.*, 2023, **13**, 9695–9705.
11 J. Gu, C.-S. Hsu, L. Bai, H. M. Chen and X. Hu, *Science*, 2019, **364**, 1091–1094.
12 Q. Zhao, Q. Wu and Z. J. Xu, *Chem. Commun.*, 2026, **62**, 692–704.
13 W. Yang, Z. Jia, B. Zhou, L. Wei, Z. Gao and H. Li, *Commun. Chem.*, 2023, **6**, 6.
14 M. Huang, R. Shi, H. Liu, W. Ding, J. Fan, B. Zhou, B. Da, Z. Gao, H. Li and W. Yang, *J. Phys. Chem. C*, 2025, **129**, 5043–5053.
15 D. Zhang, Z. Bao, Y. Chu, Z. Guo, X. Jia, Q. Jiang, H. Liu, T. Liu, T. Lu, Y. Lu, D. Devang Shah, Y. Wang, Y. Wang, Y. Wang, S. Ye, S. Ying, Z. Yu, L. Zhang, S. Zhao and H. Li, *ChemRxiv*, 2026, preprint, DOI: 10.26434/chemrxiv-2024-9lpb9.
16 S. Liang, L. Huang, Y. Gao, Q. Wang and B. Liu, *Adv. Sci.*, 2021, **8**, e2102886.
17 L. Li, S. Wu, D. Cheng, Z. J. Zhao and J. Gong, *Chem. Commun.*, 2024, **60**, 3922–3925.
18 Z. Guo, Y. Yu, C. Li, E. Campos Dos Santos, T. Wang, H. Li, J. Xu, C. Liu and H. Li, *Angew. Chem., Int. Ed.*, 2024, e202319913.
19 S. Ye, Y. Wang, H. Liu, D. Zhang, X. Jia, L. Zhang, Y. Zhang, A. Kumatani, H. Shiku and H. Li, *J. Mater. Chem. A*, 2025, **13**, 37821–37832.
20 N. Govindarajan, A. Xu and K. Chan, *Science*, 2022, **375**, 379–380.
21 Y. Zhang, Y. Wang, N. Ma, Y. Li, B. Liang, S. Luo and J. Fan, *J. Colloid Interface Sci.*, 2023, **650**, 961–971.
22 G. Zhang, B. Tan, D. H. Mok, H. Liu, B. Ni, G. Zhao, K. Ye, S. Huo, X. Miao, Z. Liang, X. Liu, L. Chen, Z. Zhang, W. B. Cai, S. Back and K. Jiang, *Proc. Natl. Acad. Sci. U. S. A.*, 2024, **121**, e2400898121.
23 S. W. Ying, Y. Wang, P. Du, Q. Wang, C. Yue, D. Zhang, Z. C. Chen, J. W. Zheng, S. Y. Xie and H. Li, *Angew. Chem., Int. Ed.*, 2025, **64**, e202511924.
24 Y. Wang, Z. Wu, Y. Jiang, D. Zhang, Q. Wang, C. Wang, H. Li, X. Jia, J. Fan and H. Li, *Adv. Funct. Mater.*, 2025, e06314.
25 Z. Jin, D. Jiao, Y. Dong, L. Liu, J. Fan, M. Gong, X. Ma, Y. Wang, W. Zhang, L. Zhang, Z. Gen Yu, D. Voiry, W. Zheng and X. Cui, *Angew. Chem., Int. Ed.*, 2024, **63**, e202318246.
26 Z. Zeng, J. Xu, Y. Zhao, J. Li, C. Du, Y. Sun and H. Xiong, *ChemCatChem*, 2024, **16**, e202400091.
27 C. Zhao, X. Dai, T. Yao, W. Chen, X. Wang, J. Wang, J. Yang, S. Wei, Y. Wu and Y. Li, *J. Am. Chem. Soc.*, 2017, **139**, 8078–8081.
28 Y. Li, W. An, Y. Wang, M. Liu, R. Guo, X. Shi, E. Dai and Y. Men, *Sci. China Mater.*, 2024, **67**, 1192–1201.